PHYSICAL REVIEW C VOLUME 22, NUMBER 4 OCTOBER 1980

Fragment production from p + Ag interactions at intermediate energies

Ray E. L. Green and Ralph G. Korteling
Department of Chemistry, Simon Fraser University, Burnaby, British Columbia V5A 1S6, Canada
(Received 10 October 1979)

Energy spectra and angular distributions have been measured for isotopically separated Li and Be and elementally separated B to Na fragments produced in reactions of 210, 300, and 480 MeV protons with Ag. These data are analyzed in terms of evaporative and nonevaporative processes. A two-parameter self-consistent evaporation calculation, normalized to ^{4}He emission, indicates a major fraction of the cross section to be nonevaporative. An analysis of the data in terms of rapidity and relativistically invariant cross section substantiates this finding. The evaporative component is weakly forward peaked and is a strongly varying function of which isotope of a given element is considered; the nonevaporative component is strongly forward peaked but varies more slowly as a function of fragment mass. Both components show behavior indicative of Coulomb barrier effects appropriate to emission from nuclides near the target. Energy integrated and total cross sections are calculated.

[NUCLEAR REACTIONS Ag(p,x); measured $\sigma(E,E_x,\theta)$, E=210, 300, 480 MeV, $x=^{6,7,8}$Li, ^{7,9,10}Be, B to Na, θ=20, 90, 160°. Deduced $\sigma(E,\theta)$ and $\sigma(E)$. Calculated evaporative and deduced nonevaporative components; invariant cross section, rapidity analysis. Spallation, fragmentation.]

I. INTRODUCTION

The introduction of solid state detector telescopes as a means of studying the production of nuclear fragments (nuclei much lighter than the target) in energetic reactions of projectiles with medium and heavy targets has greatly extended the knowledge of these reactions. The advantages and limitations of studying fragmentation with solid state telescopes are discussed at length in papers describing some of the original measurements of this type.[1-3] In particular, Ref. 2 includes extensive comparisons of this method with other experimental techniques used to study fragmentation.

Radiochemical and emulsion studies of specific fragments from a variety of targets has yielded a reasonably detailed description of these processes as a function of target mass, and solid state telescope studies have expanded on this description. Dependences on projectile type have also been studied and experiments of this nature are increasing in frequency with the advent of relativistic heavy ion facilities. An extensive review of earlier work can be found in Chap. 5 of Ref. 4. More recent work with counter telescopes is summarized in Ref. 5.

Counter telescope work on heavy fragments ($Z \geq 3$) has been primarily limited to beam energies near and above 1 GeV where the cross sections for their production are sizable. The main purpose of the experimental work described here is to study the production of these heavy fragments as a function of lower beam energies where the decrease in cross section is compensated for by the simpler kinematics of the interactions. By removing complications due to kinematics, it is easier to study reaction mechanisms for the production of these fragments. Assuming there is no strong dependence of reaction mechanism on incident energy, and we find no indication from the work described here that there is, such lower energy data may be the key to understanding fragmentation.

At lower energies, there is a recent extensive set of single particle inclusive spectra measurements on H and He fragment production by 90 MeV protons, 80 MeV deuterons, and 140 MeV ^{4}He projectiles incident on a variety of targets[6-8] and a less extensive set of such measurements on production of these light fragments by 600 MeV protons on various targets.[9] Telescope data for heavier fragments over a short range of fragment energies are available for 660 MeV protons incident on several targets for one (90°) scattering angle.[10] Telescope data on heavy fragment production induced by 720 MeV alpha particles has recently been reported with elemental, but not isotopic, fragment identification.[11] Previous studies of heavy fragment production for incident energies less than 660 MeV have been limited to radiochemical and emulsion techniques.

Since the general dependence of fragmentation on target mass is empirically known reasonably well, we have chosen to use one target and concentrate on the less well determined dependences such as those on beam energy in the region of rapidly changing cross sections and on fragment

type, energy, and emission angle. A silver target was chosen as representative of typical medium mass nuclides which exhibit statistical behavior and because it would permit us to compare our results with the considerable information available on this target at higher beam energies and also with radiochemical studies at similar beam energies. Reference 2 provides quite a complete review of previous results from work on Ag targets at beam energies near and above 1 GeV, and Refs. 3 and 5 update this material with more recent information. A summary of radiochemical cross section measurements[1,12-23] of selected light nuclei from protons incident on Ag targets is given in Fig. 1 along with our results for ^{7}Be fragments from Ag.

Previous work on the production of heavy fragments has made it clear that while the energy spectra of these fragments have the qualitative appearance of evaporation spectra, there are difficulties in obtaining quantiative fits to the data with evaporation calculations alone. This has led to proposals of other mechanisms for fragment production, e.g., Refs. 9 and 24–41, and to various modifications of evaporation calculations in an effort to make them fit the data, e.g., Refs. 1–3, 5, 11, and 42. Our previous work[43] with He fragments from Ag shows that mechanisms other than evaporation are definitely required to explain fragment production. This article shows this to be true for heavy fragments as well.

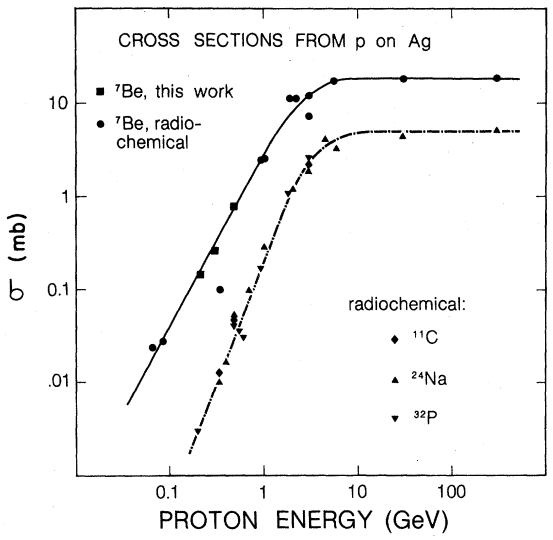

FIG. 1. Comparison of our measured ^{7}Be cross sections from p+ Ag reactions to radiochemically determined cross sections. Also shown are radiochemical determinations for three other selected fragments. Lines drawn are the authors' concept of the trends indicated. For the sake of clarity, some close lying radiochemical measurements have been averaged and displayed as one point and the ^{24}Na and ^{32}P points at two locations are offset slightly to avoid nearly complete overlap with nearby ^{11}C points.

Although one must invoke mechanisms other than evaporation in order to explain all of the data, it is clear that there is indeed an appreciable component in the data due to an evaporation process. It is our feeling that this evaporative component has not yet been adequately treated and this article presents results from a calculation which combines more of the concepts known to be important in evaporation than have been incorporated in previous calculations of heavy fragment evaporation. The details of this calculation are presented elsewhere.[44] It is considerably more elaborate (but basically more fundamental) than the previous calculations, and thus its description is tedious if one's only interest is that it provide a reasonable means of identifying (by subtraction) the nonevaporative parts of the measured fragment spectra. Results from the calculation are used in this article with minimal explanation, and interested readers are referred to the detailed description.

Experimental details concerning our single particle inclusive spectra measurements are given in Sec. II. Results of these measurements and of a two-component fitting procedure which attempts to separate the evaporative and nonevaporative components are given in Sec. III. Section IV describes a model-independent analysis of the data which demonstrates the necessity of invoking reaction mechanisms other than evaporation in order to explain the data. This analysis also provides constraints applicable to any statistical mechanisms proposed for explaning the data. Finally, the conclusions based on the information here and on more detailed calculations discussed in Ref. 44 are summarized. The single particle inclusive spectra for the measured fragments are numerically tabulated elsewhere.[45]

II. EXPERIMENTAL TECHNIQUES

The experimental work was conducted using a 152 cm diameter scattering chamber located in an external proton beam line at the TRIUMF accelerator. The electronics and data acquisition systems were in an equipment trailer approximately 40 m away. Some experimental details involved in the measurements presented in this paper have been discussed elsewhere,[43,46,47] so portions of this section are shortened summaries. Specific aspects of this experiment not discussed elsewhere are treated in somewhat more detail.

A. Incident beams, targets, and detectors

Incident beam energies of 210, 300, and 480 MeV were chosen because they spanned the energy

range of interest and were known to have reproducible beam characteristics well suited to the planned measurements. The incident beams, as measured on a zinc sulphide scintillation screen, were contained within a 1 cm diameter and were centered within 2 mm. Of more consequence, potential effects from the possible existence of a beam halo were essentially absent. Detectors have been used without difficulty 5 cm from a 2 μA beam. Target-in versus target-out singles rates in the larger volume detectors generally exceeded 10 to 1 and indicated the vast majority of the background to be target related. Incident beam currents used generally ranged from 200 nA to 2 μA and frequently were limited by limits of about 10 000 Hz imposed on the singles rates in the detectors. These limits on singles rates helped ensure good quality data.

The principal target used in this study was a commercially prepared natural silver target of measured mean thickness 2.3 mg/cm^2. It was mounted in an aluminum frame across an 8 cm by 6 cm opening, leaving a large area, free standing target after using an acetone bath to dissolve the manufacturer's backing material from the target. On a macroscopic scale, the uniformity of the target was good. However, measurement of the target thickness by the energy loss of alpha particles from an ^{241}Am source revealed, in broadened energy straggling, a significant nonuniformity on a microscopic scale. This was confirmed by examination of the target with a microscope. The straggling distribution from the alpha source measurements was inverted to yield a thickness distribution for the target. Knowledge of this thickness distribution allowed calculated energy spectra to be accurately corrected for target thickness effects before comparison with the data (by an integration over 35 differential slab thicknesses for work in the present paper). This was found to be important in determining parameters in the evaporation calculations discussed later.

The silver target also contained light mass impurities from sources such as oxidation and residual traces of backing material. These impurities yielded a background in the measurements of the energy spectra for light fragments at low fragment energies, especially for neutron deficient isotopes. A target of VYNS (85% CH_2CHCl and 15% $CH_3CO_2CHCH_2$) film ~100 μg/cm^2 thick was used to obtain an approximation to this background.

The principal detector telescope used to collect data consisted of five commercial silicon surface barrier detectors mounted on one of the rotable arms of the scattering chamber. These transmission detectors were spaced in 1 cm steps in an aluminum housing along with copper collimators and vented spacers. The acceptance cone of the telescope and the 0.16 msr solid angle subtended were determined by a 1 mm thick Cu collimator of 5 mm inner diameter at 35 cm from the target and a second 1 mm thick Cu collimator of 6 mm inner diameter 1 cm behind the first with the initial detector between these two collimators. The four data detectors in the telescope were of increasing thickness from front to back (12.9, 76, 476, and 1065 μm) and these were followed by a detector that provided a veto signal for particles not stopping in the data detectors. The first three detectors had 50 mm^2 active areas, the 1065 μm detector had a 100 mm^2 active area, and the reject detector had a 150 mm^2 active area.

A monitor telescope was mounted at a fixed angle of 90° to the beam at a distance of 25 cm from the target to the initial collimator. The geometry of the telescope was again defined by two 1 mm thick copper collimators 1 cm apart with the initial detector between them. The first collimator was of 8 mm inner diameter and the second of 10 mm inner diameter. The detectors used, in order, were 33.8 μm (100 mm^2), 262 μm (100 mm^2), and 210 μm (150 mm^2). The first two detectors were used to collect fragment data in a conventional $\Delta E, E$ mode with the 210 μm detector used as a veto counter. The second two detectors were used in a passing mode to identify ^{4}He fragments with energies between 40 and 80 MeV. This identification was done in the electronics and provided a signal which was scaled as our primary beam monitor. A polarimeter[47,48] immediately down beam of this chamber allowed normalization of the monitor telescope to known proton elastic scattering cross sections, thus providing absolute overall normalizations of the measured cross sections to ±25%. The internal relative normalizations obtained using the monitor telescope should be correct to ±5%, as discussed shortly.

B. Electronics and data acquisition

Signals from the detectors were processed in standard linear electronics. Delayed linear outputs from the amplifiers were presented to linear gates preceding the data acquisition system. These gates were opened only when signals from valid events, as determined from the logic circuitry, were present.

The linear systems were calibrated by normalizing signals generated by a precision pulse generator to signals generated by alpha particles from either a ^{212}Pb or ^{241}Am source. Once a system was normalized, no change in preamplifier, detector, or cabling from pulser, bias supply, or detector was made without renormalizing the

system. Periodic checks and adjustments of these normalizations were made over the course of a year of experimental runs. The long term stability of these normalizations was quite good, the largest change observed in a five month period being 0.6% in the 12.9 μm system while the others all changed less than 0.3%. This normalization procedure was also used for detectors thinner than the range of alpha's from the source because a small but usable fraction of full energy alpha's, presumably from scattering within the detectors, was observed.

Before each group of experimental runs, an energy calibration for each detector system was obtained by using the precision pulse generator with its appropriate normalizations. The calibration points were then fitted by a linear least-squares program and were generally found to be within one part in 2000 of the calculated curve from 2–98% of the energy range.

Relatively low load resistances of 10 MΩ were used in the bias supply lines to the detectors. This allowed reasonably accurate adjustment of the supply voltages to compensate for the IR drops in the load resistors. Thus full voltage could be maintained on the detectors as their leakage currents rose with increasing radiation damage.

An additional linear signal was generated from the prompt outputs of the amplifiers for the data detectors of each telescope. These linear signals were attenuated by varying predetermined amounts and then added in sum amplifiers. By demanding that this signal S be above a given level S_0 a logic signal $\sum$ was generated whenever the condition

$$\sum_{i=0}^{n} \frac{E_i}{E_{i0}} \geq 1$$

was met where E_i is the energy deposited in detector i and E_{i0} is the energy which when deposited in detector i alone gives $S = S_0$. For $n = 2$ cases, such as the monitor telescope, this condition defines a triangular region at the origin of a plot of ΔE vs E. The signal $\sum$ can then be used to exclude consideration of events in this region before they are presented to the data acquistion system. The situation for $n > 2$ is more complex but the same principle can be used. For our telescopes, the $\sum$ signal plus threshold requirements on ΔE signals could be used to completely exclude all ^{4}He and lighter mass fragment events from consideration while not excluding any Li isotope or heavier mass fragment events. This proved to be of considerable value in reducing the amount of time required to collect and analyze data.

Majority 2 logic on logic signals generated from single-channel analyzer (SCA) outputs for each detector was used to define possible events. When any further conditions, e.g., existence of a sum system signal $\sum$, were met, appropriately delayed SCA outputs for each detector were required to be in coincidence with the event signal before the linear gate associated with the detector was opened to allow data to pass to the data acquistion system. The resolving time required of this coincidence was typically set at 40 or 60 ns for all but the first ΔE detector of a telescope where increased time jitter required 100 to 120 ns times. Among other benefits, this timing requirement eliminated the need for separate pile-up rejection circuitry (the beam at TRIUMF has a microstructure consisting of pulses a few ns wide 44 ns apart).

An event signal generated in the logic circuitry was used to trigger the data acquistion system. This system consisted of a multiparameter analog-to-digital converter (ADC) system interfaced to a computer system. The data were processed in machine language subprograms which were controlled by a high level language main program. Input from each detector system involved in a valid event was digitized to 11-bit accuracy and recorded event by event on magnetic tape. Selected displays for monitoring purposes were also generated from the input data. Time-of-day information was recorded on the magnetic tape at intervals determined by a fixed number of events.

A set of CAMAC scalars was also interfaced to the computer system. These were used to count the various signals needed for normalization of the data and for monitoring of equipment performance. Some of these scalars were run in a multiscaling mode in which the accumulated counts for a given time period were stored as a point in a histogram display in the computer. This allowed post-run monitoring of various systems including the incident beam. Scalar values and displays were recorded on the same magnetic tape containing the event data immediately following a given experimental run.

Concurrently with data acquistion, precision pulser generated events were processed in the system at a rate of 1 Hz. These were identified on the output event tape by setting one of the optional flag bits available in the source identification portion of the computer output word associated with the various detectors.

The signals from the monitor telescope which were scaled as the primary beam monitor were generated by setting SCA levels to select events in the second detector between 5.09 and 9.54 MeV in coincidence with events in the third detector between 4.29 and 9.85 MeV. This selected ^{4}He events between 40 and 80 MeV plus ^{3}He events in a slightly differing range. Fragments of $Z \neq 2$

gave no contribution to this signal. The major source of error in this signal stemmed from the stability and reproducibility of the SCA levels and yielded a 4% uncertainty in the relative normalizations between differing runs at a given incident beam energy. The additional uncertainty from the statistical error in the number of counts scaled was always less than 1%. In those cases where there are runs with identical configurations separated in time by several months, the differences in relative normalizations have been within these errors.

C. Data reduction

The data which had been accumulated on magnetic tape were analyzed off-line at the Simon Fraser University computing center. An initial program checked and sorted the data of interest and wrote new tapes containing the data sets on which the major analyses were performed. In this initial step, the data were digitally stabilized relative to the concurrently collected pulser events (corrections were usually less than 1 part in 1000). Data which were taken during periods of questionable operation of any system could also be eliminated during this initial step by use of the time-of-day markers on the data tape; in these cases, normalization information was available from the multiscale displays.

The main features of the algorithm used to calculate particle type from the $\Delta E, E$ information have been discussed in Ref. 46 and the particle identification (PI) spectra shown there are some of those used in obtaining the data for this article. This algorithm is based on finding and integrating the appropriate Bragg curve by using the Bethe-Bloch equation with a universal effective charge term. A slightly modified algorithm was used to analyze some of the latter data; Figs. 2 and 3 show PI spectra generated with the altered version. The modification resulted from use of a different approximation to the integral involved leaving the equation

$$\Delta E = t\left|dE/dx\left(E_0 - \frac{\Delta E}{2}, Z, M\right)\right|$$

to be solved by iteration as previously (t is the ΔE detector thickness and E_0 is the energy of the fragment incident on the ΔE detector). The two advantages of the modified version were decreased computation time and elimination of the low energy cutoff needed for the thicker ΔE detectors in the original algorithm.

Figures 2 and 3 both use the same data set, which is also the same data set used for the PI spectra shown in Ref. 46. This allows easy comparisons that illustrate several points. For the

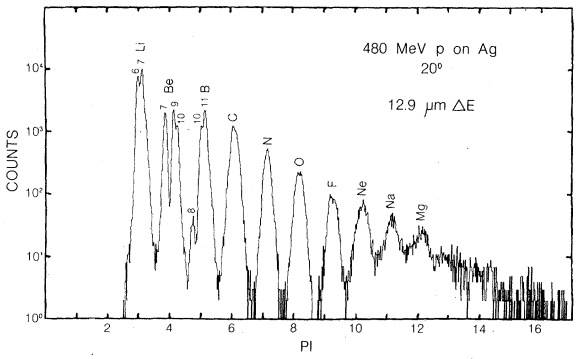

FIG. 2. Fragment particle identification spectrum resulting from use of 12.9 μm Si ΔE detector data in the algorithm discussed in the text. H and He isotopes were electronically rejected.

thin 12.9 μm ΔE, both the original and the modified algorithm yield essentially the same results. In both the original and the modified algorithm, the PI resolution is determined predominantly by the ΔE width relative to the ΔE value. Since this relative width decreases as the detector thickness increases, the PI resolution is better for the 76 μm ΔE analysis. The major difference between the 76 μm cases is that no measured data were excluded using the present version of the algorithm. Had the low energy parts of the data not been excluded in the original version, the PI resolution would have reflected inadequacies in the calculation rather than the intrinsic resolution available.

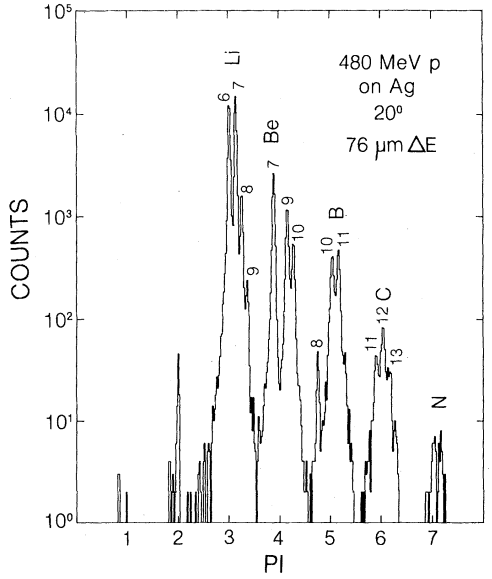

FIG. 3. Fragment particle identification spectrum resulting from use of 76 μm Si ΔE detector data in the algorithm discussed in the text. H and He isotopes were electronically rejected.

Energy spectra for a given fragment type were determined by setting windows on the calculated PI spectra using the 12.9 μm detector as ΔE and also by using the 76 μm detector as ΔE with a subsequent correction to the energy spectra for the energy loss in the 12.9 μm detector. Since the thicker ΔE gives better PI resolution, data from analyses with this detector are used where possible. However, the thicker ΔE prevents observation of the lower energy fragments, which requires data for this region to be taken from analyses with the 12.9 μm detector. With the newer version of the algorithm, the lower cutoffs used for thicker detector analyses were ^{6}Li, 22 MeV; ^{7}Li, 24 MeV; ^{7}Be, 32 MeV; ^{9}Be, 36 MeV; and ^{10} Be, 40 MeV.

The spectra were normalized to give absolute cross section information by use of the scaled signal from the monitor telescope. A dead time correction determined predominantly by the time required to digitize and process the signals was calculated by comparing the number of events presented to the data acquisition system with the number of events processed. For the present heavy fragment work ($Z \geq 3$), the dead time correction was always less than 1%. For previous He measurements,[43] it was usually 1–2% except for a few runs with corrections up to 7% and one run (consistent with others) with a 30% correction.

To correct for background from light mass impurities on the target in a self-consistent manner, spectra from the VYNS target were analyzed by the same methods used for the Ag target. Information for relative normalization of VYNS data was provided by the monitor counter so that only one arbitrary overall normalization was used at each of the three beam energies. This overall normalization was found by comparing Ag and VYNS target spectra for ^{7}Be at 20° and 90° where the majority of the very low energy ^{7}Be events from the Ag target were due to contaminants. The normalization choice was verified by analogous comparisons for the ^{6}Li spectra and, where available from previous work, ^{3}He spectra. Figure 4 indicates the magnitude of these background subtractions for the most severe case aside from the ^{7}Be case which determined the background normalization used for the figure. As the fragment energy increases, the correction required rapidly decreases. The correction also decreases as the beam energy increases and is significantly smaller for all isotopes other than ^{3}He, ^{6}Li, and ^{7}Be. For the data presented in this paper, we have excluded points falling in energy ranges where the correction leads to unreasonably large statistical uncertainties. Conclusions drawn in this work do not depend sensitively on this correction.

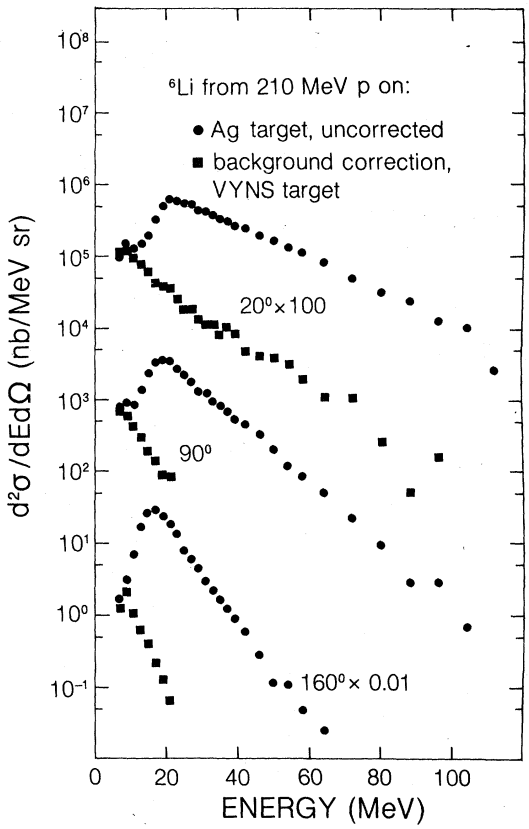

FIG. 4. Energy spectra of ^{6}Li fragments from a silver target with impurities and from a VYNS target both bombarded with 210 MeV protons. These illustrate background effects from target contaminants for an extreme case.

In those cases where background subtraction has not already determined the low energy bound on the spectra presented, we have chosen these low energy bounds to be above the region where the detection efficiency is affected by range straggling in the ΔE detector. Similarly, in those few cases where there are sufficient statistics to extend the upper energy limits for the spectra to the limits from the total telescope thickness, we limit the data presented to regions of total detection efficiency; care in this regard was more significant for previous He isotope measurements.[43]

One peculiarity of multiple ΔE detector systems deserves a word of caution. When several detector signals are being added as the E signal for $\Delta E, E$ analysis, a distortion is produced in the measured energy spectra at energies corresponding to events where the fragment stops near a gap between detectors. The effect of the dead layers on the surfaces of the detectors used in this study is not significant for the fragments observed, but the minimum energy required to trigger the appropriate SCA is typically around 1 MeV and this

TABLE I. Range of measurements made in this work and the energy-integrated differential cross sections obtained. The minimum and maximum fragment energies considered are given by E_{min} and E_{max} in MeV. The $d\sigma/d\Omega$ values are given in μb/sr. The values labeled "meas" are the integrals from E_{min} to E_{max} of the measured data. The values labeled "tot" are our estimates of the total $d\sigma/d\Omega$ based on the fitting procedure described in the text (corrections <1% are not applied). The entries for the percentage of $d\sigma/d\Omega$ due to evaporation are also taken from this fitting procedure. The values for ^{9}Be and ^{10}Be are accurate in sum but may not be accurately proportioned due to difficulties in resolving these isotopes in the measurements.

Beam energy (MeV)	Detector angle (degrees)		^{3}He	^{4}He	^{6}Li	^{7}Li	^{8}Li	^{7}Be	^{9}Be	^{10}Be	B	C	N	O	F	Ne	Na
210	20	E_{min}			10	8	24	18	16	16	18	18	24	23	24	26	30
		E_{max}			116	124	108	140	108	100	116	108	84	71	72	46	62
		$d\sigma/d\Omega$ meas			156	165	6.80	26.9	23.2	14.6	36.3	26.5	6.67	3.92	1.37	1.27	0.77
		$d\sigma/d\Omega$ tot			156	165		26.9	23.2	14.6	36.3	26.5	7.08	4.01			
		% evap			13	14		10	28	15	10	14	12	13			
	90	E_{min}	10	5	10	8	24	14	12	12	12	14	18	21	24	26	30
		E_{max}	98	108	108	100	68	100	68	68	76	68	60	63	48	46	54
		$d\sigma/d\Omega$ meas	752	17 900	57.6	56.4	2.02	9.08	10.4	4.79	13.6	12.1	3.13	1.67	0.54	0.45	0.24
		$d\sigma/d\Omega$ tot	763	17 900	57.6	56.4		9.08	10.4	4.79	13.6	12.3	3.62	2.01			
		% evap	12	80	34	38		23	54	42	22	27	23	23			
	160	E_{min}	10	5	6	6	24	12	10	12	12	14	18	21	24	26	30
		E_{max}	72	88	68	60	48	68	40	48	48	48	48	47	48	38	46
		$d\sigma/d\Omega$ meas	307	14 800	32.1	32.3	0.43	4.69	6.82	3.07	8.50	8.19	2.21	1.10	0.34	0.26	0.12
		$d\sigma/d\Omega$ tot	333	14 800	32.1	32.3		4.69	6.82	3.10	8.59	8.38	2.43	1.38			
		% evap	26	94	55	64		46	82	61	29	38	30	30			
300	20	E_{min}	4	5	8	8	36	16	12	14	12	14	22	21	24	26	30
		E_{max}	98	108	116	124	132	164	132	116	108	116	92	95	88	78	78
		$d\sigma/d\Omega$ meas	3040	28 600	237	245	9.66	44.3	42.7	22.4	67.6	49.3	14.9	8.86	3.70	3.15	1.95
		$d\sigma/d\Omega$ tot	3310	28 600	237	245		44.3	42.7	22.4	67.6	49.3	15.8	9.22			
		% evap	5	68	16	17		11	29	14	11	11	10	8			
	90	E_{min}	6	5	8	8	36	14	12	12	12	14	18	21	24	26	30
		E_{max}	98	108	116	116	92	116	92	84	84	68	60	63	64	62	54
		$d\sigma/d\Omega$ meas	1200	21 200	108	108	1.54	17.7	21.7	9.46	31.1	25.3	7.42	4.19	1.48	1.20	0.59
		$d\sigma/d\Omega$ tot	1200	21 200	108	108		17.9	21.7	9.46	31.5	26.2	8.39	5.19			
		% evap	12	84	33	36		26	57	30	21	19	18	13			
	160	E_{min}	6	5	8	8	36	12	10	12	12	14	18	21	24	26	30
		E_{max}	98	108	84	92	60	92	52	56	68	60	56	55	48	62	54
		$d\sigma/d\Omega$ meas	549	16 900	64.5	65.0	0.18	9.40	14.7	5.07	19.0	17.4	4.73	2.31	0.70	0.52	0.19
		$d\sigma/d\Omega$ tot	549	16 900	64.5	65.0		9.40	14.7	5.15	19.4	18.2	5.79	3.17			
		% evap	25	91	50	55		48	77	51	31	26	23	20			

TABLE I. (*Continued.*)

Beam energy (MeV)	Detector angle (degrees)		^{3}He	^{4}He	^{6}Li	^{7}Li	^{8}Li	^{7}Be	^{9}Be	^{10}Be	B	C	N	O	F	Ne	Na
480	20	E_{min}	4	5	6	6	36	14	10	12	12	14	18	21	24	26	30
		E_{max}	88	98	116	124	140	156	132	148	108	124	132	111	96	94	94
		$\frac{d\sigma}{d\Omega}$ meas	5210	46 600	554	608	27.7	119	116	68.1	196	166	63.6	37.4	16.7	14.5	10.8
		$\frac{d\sigma}{d\Omega}$ tot	6170	46 600	554	608		119	116	68.1	196	166	64.9	39.0			
		% evap	6	57	16	16		14	26	12	13	9	6	4			
	90	E_{min}	4	5	6	6	36	12	10	12	12	14	18	21	24	26	30
		E_{max}	98	108	116	124	108	132	108	100	100	100	92	79	88	78	78
		$\frac{d\sigma}{d\Omega}$ meas	2280	35 500	288	301	5.67	57.7	68.5	31.5	111	92.5	32.0	17.6	6.87	5.62	3.39
		$\frac{d\sigma}{d\Omega}$ tot	2320	35 500	288	301		57.7	68.5	31.9	112	95.7	36.0	21.4			
		% evap	17	76	30	30		27	42	22	22	12	10	6			
	160	E_{min}	4	5	6	6	36	8	10	12	12	14	18	21	24		
		E_{max}	98	88	92	92	76	100	84	60	76	60	60	55	56		
		$\frac{d\sigma}{d\Omega}$ meas	1200	27 400	154	161	0.91	29.1	40.6	14.2	60.3	49.0	16.0	7.57	2.54		
		$\frac{d\sigma}{d\Omega}$ tot	1200	27 400	154	161		29.1	40.6	14.6	61.9	51.9	19.4	10.2			
		% evap	31	89	50	51		54	71	45	36	22	16	12			

leads to the distortion. No loss of integrated cross section is entailed, but counts from a small region of fragment energies are observed at an energy artifically lowered by about 1 MeV. These are added to the true events of that energy. For the most part, the energy binning used in presenting the data in this article is such that we have integrated over this effect. However, in certain cases such as some of our Li spectra between 20 and 25 MeV, this effect is noticeable and one should be cognizant of the source.

III. RESULTS AND TWO-COMPONENT FITS TO THE DATA

Table I summarizes the range of data taken in this and our previous helium isotope study[43] of single particle inclusive spectra for fragments from p+Ag reactions. Data were taken at 20, 90, and 160° for the indicated fragments at each of the three incident beam energies. The range of fragment energies over which we have valid data is given by the entries E_{min} and E_{max} for each combination of incident energy, fragment type, and fragment angle. These data are tabulated in the Physics Auxiliary Publication Service of AIP.[45] The availability of the entirety of the data in tabulated form precludes the need for a large number of figures showing the measured energy spectra, and the data shown in Figs. 4 through 8 should suffice as a representative sample. As discussed in the experimental techniques section, we have chosen E_{min} and E_{max} such that we believe there to be no significant instrumental effects (aside from target thickness) on the spectra inside the indicated energy range. We also expect background effects inside these ranges to be generally minimal, except for the lighter isotopes at lower energies where E_{min} is determined by the statistical accuracy of the background subtraction. E_{max} is either a telescope range limit or, more often, is determined by insufficient numbers of events due to the small cross sections being measured.

The entries in Table I for $(d\sigma/d\Omega)_{meas}$ are the experimental $(d^2\sigma/d\Omega\, dE)$ values integrated from

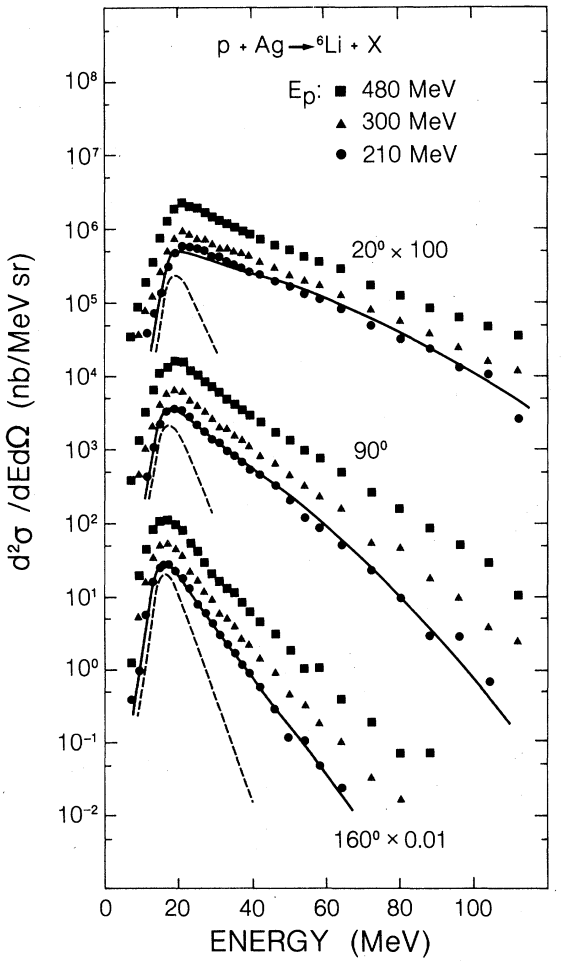

FIG. 5. Energy spectra of ^{6}Li fragments at three laboratory angles from p+ Ag interactions at three proton energies. The results of a two-component calculation described in the text are shown for the case of 210 MeV incident protons; the dashed curves are the evaporative component of the fit.

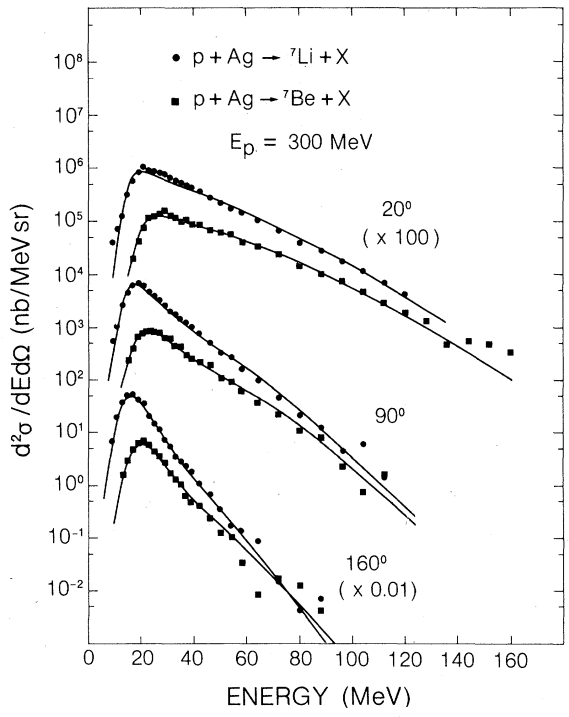

FIG. 6. Energy spectra of ^{7}Li and ^{7}Be fragments from 300 MeV proton interactions with Ag measured at three laboratory angles. The calculated curves are described in the text.

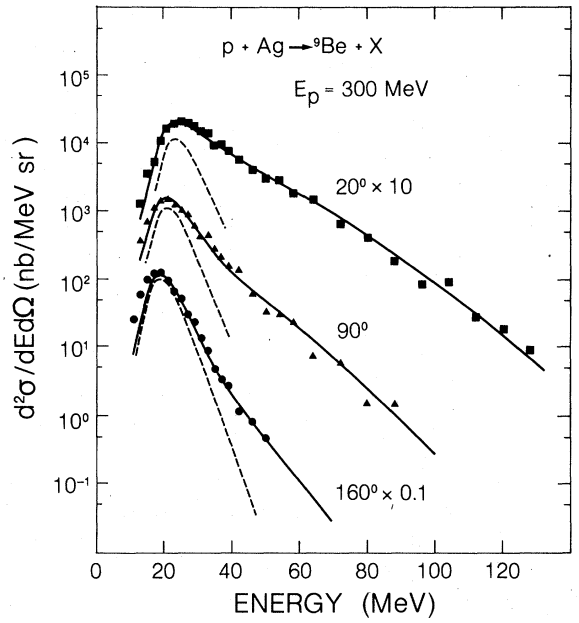

FIG. 7. Energy spectra of ^{9}Be fragments from 300 MeV proton interactions with Ag measured at three laboratory angles. The solid curves are the total two-component calculation discussed in the text, and the dashed curves are the evaporative component of this calculation.

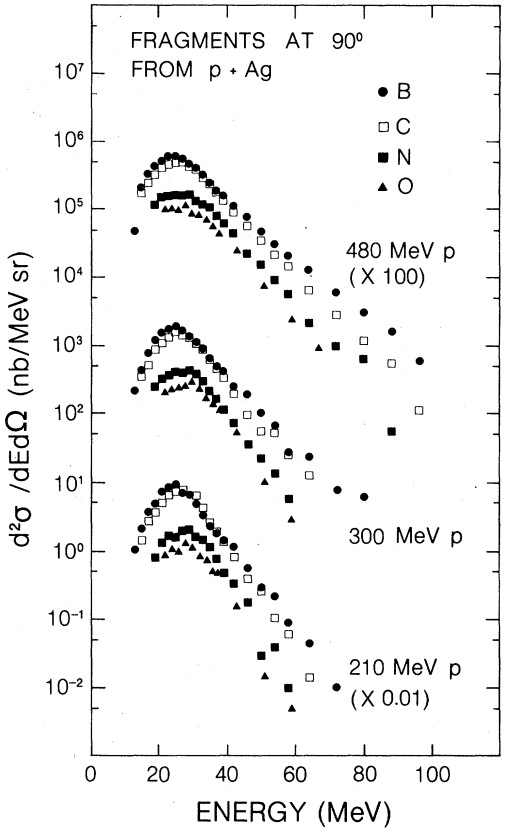

FIG. 8. Energy spectra for B, C, N, and O fragments at 90° in the laboratory as produced by p+ Ag interactions at three beam energies.

E_{min} to E_{max}. The entries for $(d\sigma/d\Omega)_{tot}$ are taken from the integral over the entire possible energy range of curves fitted to the data as described below. For those cases in which less than one percent of the cross section is believed to fall outside of the measured range, $(d\sigma/d\Omega)_{tot}$ is taken as $(d\sigma/d\Omega)_{meas}$ with no corrections applied. The percent evaporation entries are also taken from these fits and indicate the fraction of the $(d\sigma/d\Omega)_{tot}$ entries which we attribute to the evaporation component of the fits. The two quantities based on fitting the data are not tabulated for some cases because insufficient data are available to define the fits adequately. As one approaches the Na fragments, it becomes increasingly important to note that the tabulated values for $(d\sigma/d\Omega)_{meas}$ are those for the spectra as modified by target thickness effects.

A. Two-component fitting procedure

The differential energy spectra were assumed to be due to an evaporation process plus other processes whose net effect yields energy spectra whose shape at any given angle is like that of evaporation from a peculiar system with no direct physical interpretation. A detailed description of the calculation used for the evaporation component is lengthy and it will be summarized only briefly in this article. The detailed description is available elsewhere.[44] The remaining component, henceforth called the nonevaporative component, since it is clearly not true evaporation, is fitted by radically altering level densities and other parameters in our evaporation code with no requirement of uniformity from angle to angle or fragment to fragment. For the purposes of this article, we regard it as merely a convenient method of fitting a smooth curve to our data for use in interpolation and extrapolation. It is interesting that this procedure seemingly fits the nonevaporative component quite well. A somewhat related procedure,[49] which is considered to be physically plausible in terms of a hot spot model,[29,30] has been reported.

In calculating the evaporative contribution to our spectra, we attempted to find a self-consistent description of the process which described all of the fragments being emitted with one small parameter set whose only variation was with incident energy and then only for that parameter which should be strongly energy dependent. This was accomplished for the isotopically separated fragments by the calculation described in Ref. 44 with

the exception of relative normalizations which were allowed to vary up to 50% to attain the final fits. The salient features of this calculation include

(1) an inverse cross section calculation based on an optical model,

(2) a one-parameter Fermi-gas level density formula valid even when the evaporation product has an energy which is not small compared to the excitation energy,

(3) summation over all particle stable excited states of emitted fragments using appropriate statistical weights and separation energies,

(4) integration over all energies and emitting nuclei of plausible excitation energy distributions and emitting nuclei distributions, and

(5) average values of source kinematic parameters derived from the excitation energies of the evaporating systems by a fixed and plausible relation.

The calculation was constrained such that there was one global level density parameter to be determined and one excitation energy parameter to be determined for each projectile incident energy.

The calculation was normalized by selecting the level density and excitation energy distribution parameters consistent with the evaporative components of the measured ^{4}He spectra. Some weight was given to the fit of the heavier isotopes in selecting the final values since we found that, for a given incident proton energy, good ^{4}He fits were obtained over a significant range of parameter values as long as the product of the level density and excitation energy distribution parameters were approximately constant. Once the level density was determined, it was held constant for all fragment emission at all incident proton energies and the calculation was normalized at the different proton energies by adjusting the excitation energy parameter to fit the ^{4}He data at that energy. The values selected for these data are $A/10$ MeV^{-1} for the level density parameter and 21, 22, and 26 MeV for the excitation energy parameters at E_p=210, 300, and 480 MeV, respectively; these excitation energy parameters define the modified Maxwellian excitation energy distributions assumed to describe the systems when energy equilibrium is first achieved. There was no fractional Coulomb barrier used in our evaporation fits. The final adjustment of the relative normalization was used to fine tune the agreement between the data and our nonevaporative plus evaporative calculation. Calculations for the elementally resolved fragments were done in an approximation which did not retain normalization information but which did use the common evaporation parameters. Calculations for these heavy fragments are arbitrarily scaled to fit the data.

Fixing the normalization in the evaporation calculation for a given fragment fixes the evaporation component of this fragment at all angles. While these normalizations are subject to several uncertainties and should not be taken as well determined, the amounts of evaporative components at 90° and 20° relative to the amount at 160° are completely determined within the calculation. Even if the evaporative contribution at 160° were set to 100%, most fragments would still have appreciable fractions of their cross section which are not explained by our evaporation calculation. The analysis in a latter section of this paper will show that this is expected independent of the evaporation model used.

Before comparing calculations with the data, the calculated values were corrected for the known target thickness effects by the technique discussed in the section describing the target. Data in Figs. 4 through 8 are displayed without target thickness corrections while the calculated curves shown are those with corrections included. Solid curves in these figures are the total calculated fits while dashed curves (shown for only part of the cases) are the evaporative components of these fits.

B. Discussion by type of fragment emitted

1. Isotopically separated fragments

The He isotope data were reported previously[43] in connection with a model-independent analysis of the statistical component of the spectra. They are included here for completeness and because their origins are closely related to those of the heavier fragments. In particular, ^{4}He provides an easily discernible evaporative component in its spectra and this provides invaluable input for determining the parameters of the evaporation calculation. In contrast, ^{3}He is a prototype for neutron-deficient, nonevaporative fragments.

Figure 5 displays the ^{6}Li data. Data for $d^2\sigma/d\Omega dE$ for ^{7}Li versus the ^{7}Li energy are nearly identical. Cross sections for ^{8}Li are down approximately one order of magnitude in the energy range where they can be measured, and ^{9}Li cross sections are down yet another order of magnitude.

The isotopic separation using the 76 μm detector for ΔE is very good (see the PI spectra of Fig. 3). However, isotopic separation using the 12.9 μm ΔE detector is not sufficient to obtain meaningful data on ^{8}Li at low fragment energies. The separation of ^{6}Li and ^{7}Li at low energies is adequate since their spectra are similar in magnitude and shape and cross contaminations should be self-canceling. Of course, no conclusions should be based on

minute differences in these spectra at energies where the 12.9 μm detector has been used. As discussed in the experimental description, a slight spectral distortion due to the multiple ΔE system used is discernible around 22 MeV in the spectra of Fig. 5.

In Fig. 6, the spectra for ^{7}Be are compared to those of ^{7}Li for a proton incident energy of 300 MeV. Figure 7 shows the ^{9}Be spectra from 300 MeV incident protons. The ^{7}Be spectra fall off much more slowly as a function of fragment energy than the ^{7}Li or the other Be isotope spectra. This is characteristic of neutron deficient fragments in this and the higher energy[1-3,5] studies.

The identification of ^{7}Be fragments is unambiguous since ^{6}Be and ^{8}Be are particle unstable. The separation of ^{9}Be and ^{10}Be fragments is good for the 76 μm ΔE but marginal for the 12.9 μm ΔE detector. Consideration of energy regions where there are available spectra based on identifications from both alternatives indicates that when using the 12.9 μm ΔE we generally attribute more of the actual ^{9}Be to ^{10}Be than vice versa and may be underestimating the ^{9}Be cross section by amounts ranging up to 10 percent. This information could be used to reset the 12.9 μm ΔE particle identification windows to achieve better overlap with the 76 μm ΔE data, but there is no assurance from the data that this overlap extrapolates into the region of interest with an accuracy significantly better than the above uncertainty. Cross sections for ^{11}Be emission are significantly smaller and our ^{7}Be, ^{9}Be, and ^{10}Be spectra represent the vast majority of the Be fragments produced.

2. *Fragments separated by elements only*

Figure 8 shows spectra for B, C, N, and O fragments at 90° for all three incident beam energies. These fragments are well resolved by element but cannot be isotopically separated in the experiment described here (with the exception of the highest energy B and C fragments where statistics do not warrant it). The 12.9 μm ΔE detector is thin enough that measured spectra for these fragments include the energies at which the cross sections are at their maxima. This is important in determining meaningful fits to the data.

Without isotopic separation, the evaporation calculation has less significance than for lighter fragments. However, the calculation is still useful for extrapolating the data and these spectra have been fitted by the procedure already described under the assumption that the emitted fragment is the most stable isotope. As with lighter fragments, the calculation is unable to account for significant amounts of their cross section.

The F and Ne fragments are clearly separated but the low energy Na fragments may include some contamination from Mg fragments. The general behavior of these fragments appears to be a simple continuation of trends in the lighter fragments. However, the energy ranges over which data are available do not warrant an extensive effort to fit these data with our present parametrization. We thus tabulate only the experimental results in Table I and in the compilation of energy spectra in the Physics Auxiliary Publication Service.[45] Potential users of these data are reminded that no target thickness corrections have been applied.

C. Angular distributions, integrated cross sections, and beam energy dependence

Figure 9 shows the energy-integrated angular distributions for fragments ^{3}He through O from 300 MeV protons incident on Ag. The total $d\sigma/d\Omega$ as calculated from our fitting procedure has been used and the two components of this fit are shown

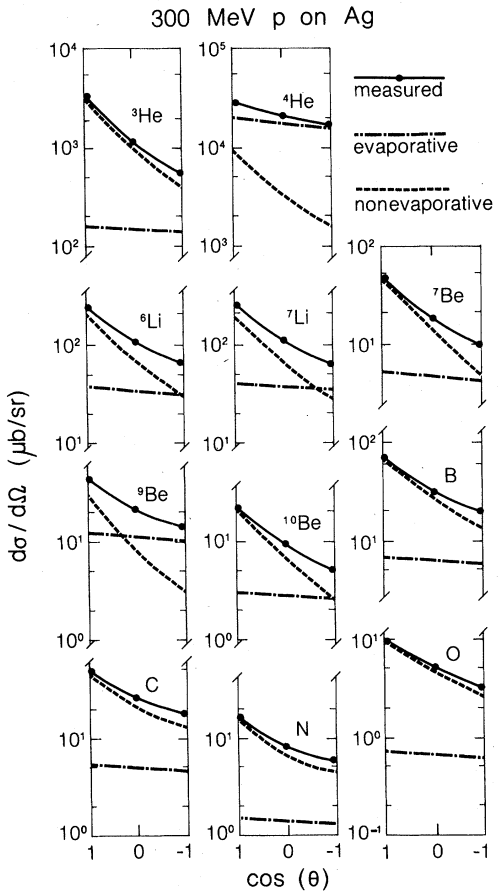

FIG. 9. Laboratory angular distributions of fragments from p+ Ag interactions at 300 MeV. Curves shown are for our two-component fits to the data with each component and the total displayed separately.

TABLE II. Cross sections in μb for fragments produced in p + Ag reactions at three incident beam energies as calculated from the measured differential cross sections by two methods described in the text. Numbers in parentheses are those obtained by applying the second method to the measured data without a correction for differential cross section falling outside the energy range of our measurements; where these values are not given, such losses are believed to be less than one percent. The values for ^{9}Be and ^{10}Be are accurate in sum but may not be accurately proportioned due to inadequate experimental resolution.

Beam energy (MeV)		210		300		480	
Fragment	Integration method	Exp fit	Hist [( ) = meas]	Exp fit	Hist [( ) = meas]	Exp fit	Hist [( ) = meas]
^{3}He				18 400	19 700	35 300	37 700
					(18 800)		(34 500)
^{4}He				274 000	276 000	453 000	456 000
^{6}Li		886	953	1 550	1 630	3 930	4 030
^{7}Li		895	974	1 570	1 650	4 170	4 310
^{7}Be		144	156	265	281	801	828
^{9}Be		151	160	305	317	907	922
^{10}Be		78	86	138	146	445	460
B		210	226	450	471	1 490	1 510
					(467)		(1 500)
C		178	187	364	377	1 270	1 290
			(185)		(369)		(1 260)
N		51	53	116	121	481	491
			(48)		(108)		(451)
O		28	30	70	72	284	289
			(26)		(61)		(252)

separately for each fragment. Each component and the total are shown with a fit of the form $\exp(a + b\cos\theta + c\cos^2\theta)$.

From Fig. 9 and similar figures at other incident energies, angle integrated cross sections may be estimated by several means. We choose two and use their comparison to illustrate the effects of the analysis procedure on the determination of σ. First is to use values obtained by integrating our fits to the $\cos\theta$ dependence. Second is to use histograms taking values of $d\sigma/d\Omega$ for $\cos\theta$ between 1 and $\frac{1}{2}$ from the $\theta = 20°$ data points, between $\frac{1}{2}$ and $-\frac{1}{2}$ from the $\theta = 90°$ points, and between $-\frac{1}{2}$ and -1 from the $\theta = 160°$ points. The latter means has been used for both $(d\sigma/d\Omega)_{\text{tot}}$ and $(d\sigma/d\Omega)_{\text{meas}}$ in order to illustrate instrumental effects on the determination of σ. Results are tabulated in Table II. Statistical errors are negligible. The overall normalization error is the ±25% from systematic uncertainty due to our monitoring technique. Our tabulated ^{7}Be values are in agreement with the systematics of most radiochemical measurements[1,12-23] as can be seen from Fig. 1.

The dependence of fragment spectra on incident beam energy is predominantly one of overall magnitude, as indicated in Tables I and II. The shapes of spectra for a given fragment remain very similar, showing only minor changes. The approximately exponential decrease in $d^2\sigma/d\Omega\, dE$ with increasing fragment energy above the evaporation peak becomes less steep only very slowly as a function of increasing beam energy. For the fragments up to boron, this change in slope is more pronounced in the 90° and 160° spectra than in the 20° spectra. Beyond carbon, the change at 20° becomes comparable to that at 90° while the change at 160° becomes less pronounced.

The positions of the maxima in the energy spectra at a given angle are the same within an MeV for all three incident beam energies. The position of the maxima at 90° for the ^{4}He spectra is the same as that reported[2] for ^{4}He from 5.5 GeV protons incident on silver. The maxima at 90° for our Li and Be isotopes are 1 to 2 MeV higher than those listed for the 5.5 GeV data, but direct comparison is difficult since we have not adjusted our data to compensate for target thickness effects. It appears that the maxima in single particle inclusive spectra are controlled by the Coulomb barrier and that this barrier is affected little by differences in incident proton energy from 0.2 to 5.5 GeV. Our two-component fitting procedure yields good fits to the 5.5 GeV ^{4}He data using a reasonable extrapolation of the excitation energy parameter values found for the work here. In particular, the evaporative component requires no use of fractional Coulomb barriers in contrast to the original[2] analysis.

IV. ANALYSIS USING INVARIANT CROSS SECTIONS AND RAPIDITIES

The failure of evaporation calculations to explain the entirety of fragment production from both energetic proton interactions and relativistic heavy ion interactions with target nuclei has been apparent for some time. As a result, a number of other mechanisms for fragment production have been proposed in the literature of this field. Some of these mechanisms are direct in nature, Refs. 31–35, for example; others are statistical in nature, Refs. 9 and 24–26, for example; and others are more exotic, Refs. 27, 28, and 37–41, for example. In this section, we apply to our data a model-independent analysis which is useful in studying the statistical components of our spectra. The technique is described in more detail in Ref. 43 and is an extension of techniques explored in earlier relativistic heavy ion work.[39] Related techniques are being used with increasing frequency in relativistic heavy ion work and have also been applied to previous high energy proton work.[38,50-54]

Figure 10 shows our ^{7}Li, ^{7}Be, and C data for 480 MeV incident protons plotted as sets of data

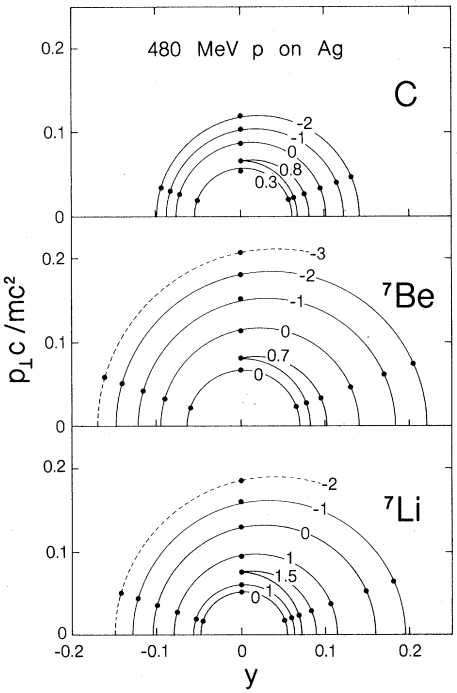

FIG. 10. Sets of data points of constant invariant cross section in the $(y, p_\perp c/mc^2)$ plane for C, ^{7}Be, and ^{7}Li fragments from 480 MeV protons incident on Ag. Fits for isotropic emission from sources moving in the beam direction are shown with labels indicating the $\log_{10}$ of the invariant cross section in nb/[(MeV/c)(MeV sr)].

points of constant relativistically invariant cross section $(1/p)(d^2\sigma/d\Omega\, dE)$ in the $(y, p_\perp c/mc^2)$ plane where

$$y = \tfrac{1}{2}\ln[(W + p_\parallel c)/(W - p_\parallel c)]$$

is the fragment's rapidity and $W, p_\parallel$ and $p_\perp$ are its total energy (including rest mass mc^2), parallel momentum, and perpendicular momentum. For the combined C isotopes, the mass of ^{12}C has been used in the calculations. Lines which intersect the negative rapidity axes are fits to the data assuming isotropic emission from sources moving in the beam direction. They are labeled with the base ten logarithm of the invariant cross section of the data points they intersect. These and similar fits are used as input to the remainder of the analysis as in our previous He work.[43] Dashed lines are fits using 90° and 160° data points, while other fits use the 20° and 160° data points. The remaining three contour levels shown are for the maximum values of the invariant cross section at 90° for each fragment. The shapes of these last three contours are not well defined by the present data and the points have arbitrarily been fitted with the appropropriate curves for isotropic emission; these curves are useful in conveying the nature of the data but are not used in any further analysis. Values of the parameters used in these calculations are taken from smooth curves which, when corrected for target thickness effects, yield good fits to the actual momentum versus invariant cross section data.

The amount by which the 90° points deviate from the isotropic fits based on the 20° and 160° points provides a measure of how well the assumption of isotropy holds. As was found in a similar analysis[50] (equivalent in the nonrelativistic limit applicable to these data) of fragments from 5.5 GeV protons on U, isotropic contours fit the data quite well except for the previously analyzed case[43] of ^{3}He. The most significant variation in these fits is in the rapidities about which these isotropic contours are centered. For a given value of invariant cross section, we shall define the rapidity about which the fit to the 20 and 160° data points is centered as β_s and refer to it as the effective source velocity associated with the given contour (β_s is actually an effective source rapidity and is equivalent to velocity only if nonrelativistic). A true one-to-one correspondence of source velocities and invariant cross section is of course not feasible because of the distributed nature of the true source velocities and the various reaction mechanisms involved. The significance of β_s in light of the distributions involved is discussed in Ref. 43 (where this parameter is called simply s).

Figure 11 shows invariant cross sections versus

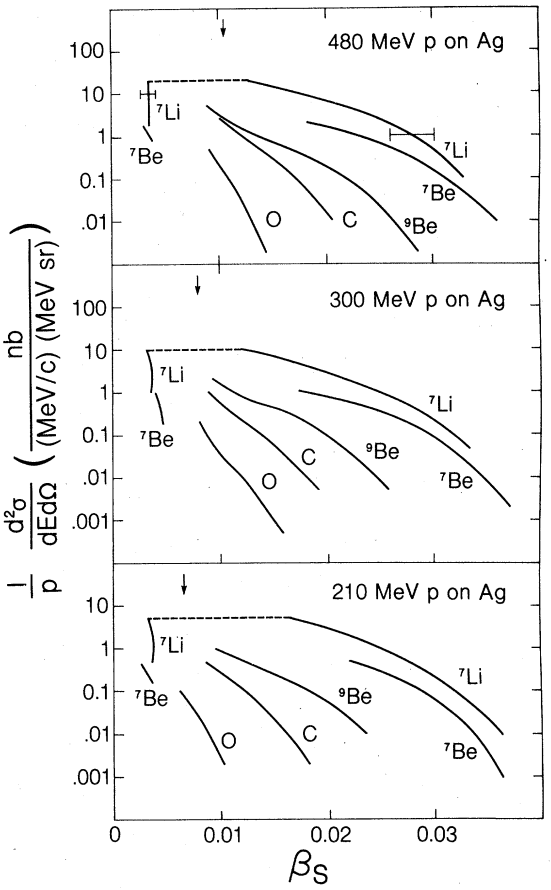

FIG. 11. Invariant cross section versus effective source velocity β_s as defined by fitting isotropic distributions from moving sources to 20° and 160° data points of the given invariant cross section (as in Fig. 10) for ^{7}Li, ^{7}Be, ^{9}Be, C, and O from 210, 300, and 480 MeV protons incident on Ag. The arrows indicate the velocities of the p+Ag compound systems. Uncertainties in relative normalizations yield errors in this analysis whose typical magnitudes are indicated on the ^{7}Li curves for the 480 MeV case.

effective source velocity β_s for several of our measured fragments at all three incident proton energies. Error bars corresponding to the uncertainty in relative normalization between angles are shown on the ^{7}Li curves for the 480 MeV case, and these are representative of the errors for all cases. The data at low β_s values (shown for ^{7}Li and ^{7}Be only since the others are similar) are derived from those parts of the energy spectra at energies below those corresponding to the maxima in the distributions; these low β_s groups give a general indication of the appropriate values, but the errors in β_s are larger than the structure in the shapes of these curves and neither these structures nor differences between fragment types have significance for these low β_s groups. The high β_s curves correspond to the high energy portions of the fragment spectra and the range of β_s values encompassed here leads to interesting constraints on statistical models.

Coupling of kinematic limits due to the incident proton energies involved with the β_s values derived from fragment data is discussed in Ref. 43. Applied to the data in Fig. 11, these arguments yield conclusions similar to those of this previous He isotope work. For example, under the assumption that the entire momentum of the incident proton is transferred to the emitting system, values of $\beta_s = 0.02$ imply part of the systems assumed to be statistically emitting the fragments must have masses less than 36, 44, and 58 u for 210, 300, and 480 MeV incident protons, respectively. Even in the extremely unlikely case at the absolute kinematic limits where all other matter is ejected at 180° to the incident beam, values of $\beta_s = 0.03$ are consistent with statistical emission of 75 MeV fragments (a typical energy associated with β_s values in this region) only if some of the systems have masses less than 0.83, 0.91, and 0.96 times the target mass for 210, 300, and 480 MeV incident protons respectively. Evaporation from a fully equilibrated nucleus with a mass near the target mass is thus ruled out as an explanation for the entirety of the fragments observed, independent of the evaporation model assumed. The increasing mass limits as the beam energy increases shows the importance of using modest beam energies for this type of argument.

Figure 11 displays information on β_s in such a way that the relative proportion of systems having a given β_s is apparent, but it does not display correlations between the fragment kinematics and source kinematics. An interesting correlation between fragment and source kinematic properties is discussed in Ref. 50 where the relation is found to hold for a variety of initial systems. Figure 12 shows part of our data displayed in terms of the appropriate variables β_s and β_r, where β_r is the radial velocity (in units of c) of the fragment in the source frame having the given β_s. As in the previous work, we find the relation between β_s and β_r to be nearly identical for all fragments except low energy ^{4}He. In fact, it is nearly the same relation previously found for fragments from 5.5 GeV p on U as can be seen from the dashed line taken from Ref. 50 for the locus about which the various β_r versus β_s curves were located. The incident energies involved in the data discussed in Ref. 50 are too high to successfully apply the kinematic arguments used here and in Ref. 43 to limit evaporation as a sole explanation of the data, but the authors of Ref. 50 argue that the data they analyze is not from a thermal type of source since

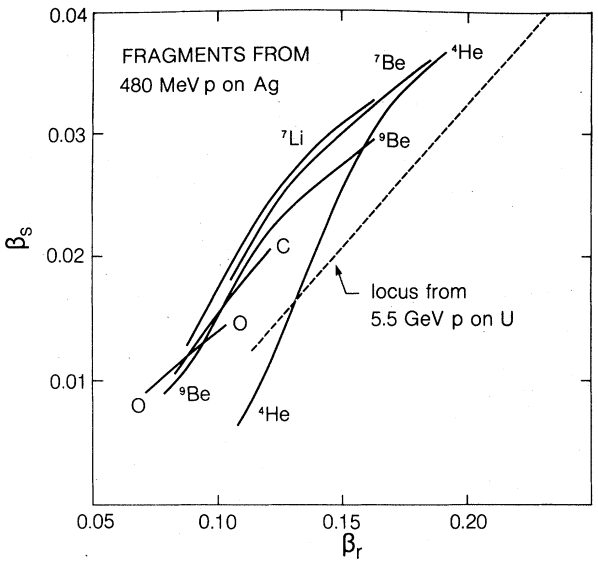

FIG. 12. Effective source velocity versus fragment radial velocity for ^{4}He, ^{7}Li, ^{7}Be, ^{9}Be, C, and O fragments from 480 MeV protons incident on Ag. The velocities β_r and β_s are taken from fits to the data such as those in Fig. 10. The previous relation found by Ref. 50 for fragments except ^{4}He from 5.5 GeV protons incident on U is indicated by the dashed line.

fragment emission from a source characterized by β_s appears to involve a characteristic radial velocity β_r instead of a characteristic energy as one would expect from a thermal source.

V. SUMMARY AND CONCLUSIONS

The general shapes of the inclusive particle spectra presented here are similar to those obtained at higher beam energies, even though the total cross sections are rapidly rising functions of beam energy for beams under a GeV. Spectra in all cases have exponentially decreasing high energy components reminiscent of evaporation spectra. The positions of the maxima in the spectra are independent of incident beam energy and have values implying they are governed by a Coulomb barrier appropriate to nuclides near the silver target. However, we have been able to show that a major fraction of the cross section cannot be attributed to the conventional evaporation mechanism by both the inability of our evaporation calculation to fit the data in a self-consistent way and by the results of an analysis of source rapidities implied by the data. When our evaporation plus nonevaporation calculation is extrapolated to 5.5 GeV incident protons, consistent and similar agreement with data from Ref. 2 is obtained. In general then, on the basis of single particle inclusive spectra, there appears to be no evidence for radical changes in the mechanisms for production of fragments as the incident beam energy is changed from 0.2 to 5.5 GeV, but there is strong evidence of major nonevaporative processes involved at all incident energies.

When the data are analyzed in terms of evaporative and nonevaporative components we find that whereas the evaporative component is strongly dependent on which isotope of a given element is considered (reflecting the relative separation energies) and is mildly forward peaked due to the source kinematics, the nonevaporative component is a more slowly varying function of fragment mass but is highly forward peaked in all cases. In fact, the varying shapes of the spectra for different isotopes of a given element are largely due to the changes in the relative amounts of evaporation involved. However, both components are governed by the Coulomb barrier; the evaporative component is affected by the total barrier, whereas the nonevaporative component seems to be affected by ~75% of the barrier expected for emission from a nucleus near to the target. It is also readily apparent that with the larger number of emitted particles and the stronger dependence of the heavier fragments on evaporative emission conditions, the study of heavy fragment emission is a much more stringent test of the evaporation process. As is discussed in our detailed description of the evaporation calculation,[44] these data have already suggested that the excitation energy distribution required to explain the evaporation component is considerably lower than that predicted by the conventional cascade calculations to be present at the end of the cascade step.

Finally, these inclusive particle spectra can aid in the determination of the physical parameters of a number of the models currently suggested for particle emission. In some cases the models may not explain the single particle inclusive data for any physically reasonable choice of parameters. In one such case involving the quasi-two-body scaling model[31] used to explain backward proton emission, the model failed when applied to ^{4}He emission.[35] In other cases where physically reasonable parameters are found for the models, these can be used in making further predictions which can then be tested in more selective experiments. The greater restraints imposed on various models by measurements of the emission of multinucleon particles, it is hoped, will be an aid in separating the probable from the plausible models.

ACKNOWLEDGMENTS

This work was supported by the Natural Sciences and Engineering Research Council of Canada.

The authors greatly appreciate a critical reading of the manuscript by K. P. Jackson. We wish to thank N. Bohna for her help in processing the data through the Simon Fraser University computing center and A. Seamster and L. Church for their assistance in the early stages of the experimental program. We acknowledge with thanks the help received from the operations staff of TRIUMF in obtaining the proton beams used in this experiment.

[1]A. M. Poskanzer, G. W. Butler, and E. K. Hyde, Phys. Rev. C 3, 882 (1971).
[2]E. K. Hyde, G. W. Butler, and A. M. Poskanzer, Phys. Rev. C 4, 1759 (1971).
[3]R. G. Korteling, C. R. Toren, and E. K. Hyde, Phys. Rev. C 7, 1611 (1973).
[4]K. Kikuchi and M. Kawai, *Nuclear Matter and Nuclear Reactions* (North-Holland, Amsterdam, 1968), pp. 217–314.
[5]G. D. Westfall, R. G. Sextro, A. M. Poskanzer, A. M. Zebelman, G. W. Butler, and E. K. Hyde, Phys. Rev. C 17, 1368 (1978).
[6]J. R. Wu, C. C. Chang, and H. D. Holmgren, Phys. Rev. C 19, 698 (1979).
[7]J. R. Wu, C. C. Chang, and H. D. Holmgren, Phys. Rev. C 19, 370 (1979).
[8]J. R. Wu, C. C. Chang, and H. D. Holmgren, Phys. Rev. C 19, 659 (1979).
[9]J. P. Alard, A. Baldit, R. Brun, J. P. Costilhes, J. Dhermain, J. Fargeix, L. Fraysse, J. Pellet, G. Roche, J. C. Tamain, A. Cordaillat, and A. Pasinetti, Nuovo Cimento 30A, 320 (1975).
[10]V. I. Bogatin, V. F. Litvin, O. V. Lozhkin, N. A. Perfilov, and Yu. P. Yakovlev, Nucl. Phys. A260, 446 (1976).
[11]T. C. Schweizer, R. R. Doering, S. T. Thornton, L. C. Dennis, K. R. Cordell, and R. L. Parks, Phys. Rev. C 19, 1408 (1979).
[12]L. Marquez and I. Perlman, Phys. Rev. 81, 953 (1951).
[13]A. A. Caretto, J. Hudis, and G. Friedlander, Phys. Rev. 110, 1130 (1958).
[14]E. Baker, G. Friedlander, and J. Hudis, Phys. Rev. 112, 1319 (1958).
[15]I. Dostrovsky, Z. Fraenkel, and J. Hudis, Phys. Rev. 123, 1452 (1961).
[16]V. P. Crespo, J. M. Alexander, and E. K. Hyde, Phys. Rev. 131, 1765 (1963).
[17]G. N. Simonoff and C. Vidal, Phys. Lett. 20, 30 (1966).
[18]M. S. Lafleur, N. T. Porile, and L. Yaffe, Can. J. Chem. 44, 2749 (1966).
[19]R. G. Korteling and A. A. Caretto, Jr., J. Inorg. Nucl. Chem. 29, 2863 (1967).
[20]S. Katcoff, H. R. Fickel, and A. Wyttenbach, Phys. Rev. 166, 1147 (1968).
[21]J. Hudis, Phys. Rev. 171, 1301 (1968).
[22]R. G. Korteling and R. Kiefer, Phys. Rev. C 2, 957 (1970).
[23]N. T. Porile, G. D. Cole, and C. R. Rudy, Phys. Rev. C 19, 2288 (1979).
[24]M. Blann, Annu. Rev. Nucl. Sci. 25, 123 (1975).
[25]G. Mantzouranis, D. Agassi, and H. A. Weidenmüller, Phys. Lett. 57B, 220 (1975).
[26]J. R. Wu and C. C. Chang, Phys. Rev. C 17, 1540 (1978).
[27]S. T. Butler and C. A. Pearson, Phys. Rev. 129, 836 (1963).
[28]H. H. Gutbrod, A. Sandoval, P. J. Johansen, A. M. Poskanzer, J. Gosset, W. G. Meyer, G. D. Westfall, and R. Stock, Phys. Rev. Lett. 37, 667 (1976).
[29]R. Weiner and M. Weström, Nucl. Phys. A286, 282 (1977).
[30]P.-A. Gottschalk and M. Weström, Nucl. Phys. A314, 232 (1979).
[31]S. Frankel, Phys. Rev. Lett. 38, 1338 (1977).
[32]N. S. Chant and P. G. Roos, Phys. Rev. C 15, 57 (1977).
[33]R. D. Amado and R. M. Woloshyn, Phys. Rev. Lett. 36, 1435 (1976).
[34]H. J. Weber and L. D. Miller, Phys. Rev. C 16, 726 (1977).
[35]D. H. Boal and R. M. Woloshyn, Phys. Rev. C 20, 1878 (1979).
[36]S. T. Thornton, K. R. Cordell, L. C. Dennis, R. R. Doering, and T. C. Schweizer, Phys. Rev. C 19, 913 (1979).
[37]G. D. Westfall, J. Gosset, P. J. Johansen, A. M. Poskanzer, W. G. Meyer, H. H. Gutbrod, A. Sandoval, and R. Stock, Phys. Rev. Lett. 37, 1202 (1976).
[38]J. Gosset, J. I. Kapusta, and G. D. Westfall, Phys. Rev. C 18, 844 (1978).
[39]J. Gosset, H. H. Gutbrod, W. G. Meyer, A. M. Poskanzer, A. Sandoval, R. Stock, and G. D. Westfall, Phys. Rev. C 16, 629 (1977).
[40]H. G. Baumgardt, J. U. Schott, Y. Sakamoto, E. Schopper, H. Stöcker, J. Hofmann, W. Scheid, and W. Greiner, Z. Phys. A 273, 359 (1975).
[41]A. M. Poskanzer, R. G. Sextro, A. M. Zebelman, H. H. Gutbrod, A. Sandoval, and R. Stock, Phys. Rev. Lett. 35, 1701 (1975).
[42]A. M. Zebelman, A. M. Poskanzer, J. D. Bowman, R. G. Sextro, and V. E. Viola, Jr., Phys. Rev. C 11, 1280 (1975).
[43]R. E. L. Green and R. G. Korteling, Phys. Rev. C 18, 311 (1978).
[44]R. E. L. Green and R. G. Korteling, TRIUMF Report No. TRI-PP-79-30 (1979).
[45]See AIP document PRVCA-22-1594-16 for 16 pages of numerically tabulated histograms of the single particle inclusive spectra measured in the work discussed in this article and in Ref. 43. Order by PAPS number and journal reference from American Institute of Physics, Physics Auxiliary Publication Service, 335 E. 45 St., New York, N. Y. 10017. The price is $1.50 for microfiche, or $5 for photocopies. Airmail additional. Make check payable to American Institute of Physics.
[46]A. G. Seamster, R. E. L. Green, and R. G. Korteling, Nucl. Instrum. Methods 145, 583 (1977).
[47]TRIUMF User's Handbook, pp. 4-31 to 4-35 (unpublished).

[48]C. Amsler, D. Axen, J. Beveridge, D. V. Bugg, A. S. Clough, R. Dubois, J. A. Edgington, D. Gibson, R. Keeler, G. A. Ludgate, C. J. Oram, J. R. Richardson, L. P. Robertson, and N. M. Stewart, J. Phys. G 4, 1047 (1978).
[49]T. Nomura, H. Utsunomiya, T. Motobayashi, T. Inamura, and M. Yanokura, Phys. Rev. Lett. 40, 694 (1978).
[50]P. B. Price and J. Stevenson, Phys. Lett. 78B, 197 (1978).
[51]K. L. Wolf, H. H. Gutbrod, W. G. Meyer, A. M. Poskanzer, A. Sandoval, R. Stock, J. Gosset, C. H. King, G. King, N. V. Sen, and G. D. Westfall, Phys. Rev. Lett. 42, 1448 (1979).
[52]S. Nagamiya, L. Anderson, W. Brückner, O. Chamberlain, M.-C. Lemaire, S. Schnetzer, G. Shapiro, H. Steiner, and I. Tanihata, Phys. Lett. 81B, 147 (1979).
[53]J. Randrup, Phys. Lett. 76B, 547 (1978).
[54]A. S. Goldhaber and H. H. Heckman, Annu. Rev. Nucl. Part. Sci. 28, 161 (1978).